Characterization and Modeling of Nonlinearities in In-Plane Gap Closing Electrostatic Energy Harvester

Sukhdeep Kaur, Einar Halvorsen, *Member, IEEE*, Oddvar Søråsen, and Eric M. Yeatman

***Abstract*— This paper investigates in detail a micro scale in-plane gap closing electrostatic energy harvester with strong nonlinearities in squeeze-film damping, electromechanical coupling, and impacts on end-stops. The device shows softening response on increasing the bias voltage and saturation behavior on impact with end-stops at high enough acceleration amplitude. We demonstrate that a lumped model can adequately describe the measured nonlinear behavior for a range of operating conditions with nonlinear fluid damping force and impact force included in the model. While modeling capacitances, a finite-element method (FEM) is used to analyze fringing field effects on the capacitance variation for gap closing electrodes. The nominal capacitance is obtained from FEM analysis, for a range of under-cut values in the fabrication process treated as a free parameter in the model. The device modeled for linear and nonlinear squeeze-film damping force highlights the importance of nonlinear damping force to understand the device behavior over the range of operating conditions. With the compliant end-stops treated as spring-dampers and with proper choice of end-stop damping-coefficient, the model successfully captures the end-stop nonlinearities for a particular operating point and reproduces the dynamic pull-in phenomena at 8 V bias, and rms acceleration 0.6 *g*, as observed in the experiments. Thus, the model described in this paper reproduces the subtle nonlinear effects dominating the dynamics of an in-plane gap closing electrostatic energy harvester. [2015-0107]**

***Index Terms*— Electrostatic devices, energy harvester, nonlinear systems, vibrations.**

I. Introduction

VIBRATION energy harvesters are gaining popularity as a possible alternative to batteries. The exhaustible nature of the batteries has encouraged researchers to exploit renewable energy sources for powering the electronics. Over the years, research has been carried out to harness electric energy by several transduction mechanisms from vibrational sources, e.g. aircraft, cars, engines, etc. Based on the transduction mechanism, energy harvesters are basically of three types: electromagnetic, piezoelectric and electrostatic [1]–[10].

Manuscript received April 21, 2015; revised July 27, 2015; accepted August 13, 2015. Date of publication September 8, 2015; date of current version November 25, 2015. This work was supported by the Research Council of Norway under Grant 191282. Subject Editor X. Wang.

S. Kaur and E. Halvorsen are with the Department of Micro and Nano System Technology, Buskerud and Vestfold University College, N-3184 Borre, Norway (e-mail: sukhdeep.kaur@hbv.no; einar.halvorsen@hbv.no).

O. Søråsen is with the Department of Informatics, University of Oslo, N-0373 Oslo, Norway (e-mail: oddvar@ifi.uio.no).

E. M. Yeatman is with the Department of Electrical and Electronic Engineering, Imperial College London at South Kensington Campus, London SW7 2AZ, U.K. (e-mail: e.yeatman@imperial.ac.uk).

Color versions of one or more of the figures in this paper are available online at http://ieeexplore.ieee.org.

Digital Object Identifier 10.1109/JMEMS.2015.2470112

While based on motion of the proof mass relative to the substrate, electrostatic energy harvesters are conventionally called out-of-plane gap closing [11], [12], in-plane gap closing [8], [9], [13], and in-plane overlap varying [7], [14], though other varieties are possible [15], [16].

Vibration energy harvesters can operate linearly or nonlinearly depending on the device type and the amplitude of the proof mass. Among these, nonlinear energy harvesters are gaining popularity as they can widen the harvester bandwidth [7]–[10]. Nonlinearities can be designed in the stiffness of the structure as in [10] and [17] or they can also appear as side effects of otherwise required design features, for example the impact of the proof mass on end-stops limiting the motion [3], [14]. Even if the proof mass moves according to linear equations of motion between the end-stops, the behavior changes abruptly as it impacts the end-stops [18].

Guillemet et al. presented an analytical model to optimize the efficiency of an electrostatic out-of-plane gap closing vibration energy harvester with a limitation on the output voltage [12]. They also discussed the electrostatic instability (pull-in phenomena) as the main limiting factor for a given resonator. P. Miao et al. fabricated an out-of-plane inertial vibration scavenging micro-generator suitable for medical applications [6]. In that device, stiff end-stops were utilized as charging and discharging studs for a moving electrode in a variable capacitor geometry. G. Despesse et al. investigated an in-plane gap closing energy conversion macrostructure, fabricated in bulk tungsten alloy, with high electrical damping [19]. P. Basset et al. studied the discrepancy between experimental and simulated data at high voltages and high acceleration amplitude in an in-plane gap closing electrostatic energy harvester [13]. Nonlinear damping due to the gas film between the electrodes was hypothesized as one of the reasons for the discrepancy, but was not introduced in their model.

R. Guillemet et al. reported a batch fabricated electrostatic in-plane gap closing energy harvester [20]. Its performance was limited by the achievable maximum capacitance. In the experiments, this capacitance differs from the design-estimates based on parallel electrode-sidewalls. The under-cut of comb-finger electrodes arising from the fabrication process drastically decreased the maximum capacitance.

The in-plane gap closing transducer is emerging as a popular type of energy harvester. Experiments show that this transducer type can achieve very effective conversion, but also that it has large nonlinear parasitic damping and is rather sensitive to processing related effects on structure that affect the capacitance [13], [21]. These matters need to be adequately modeled

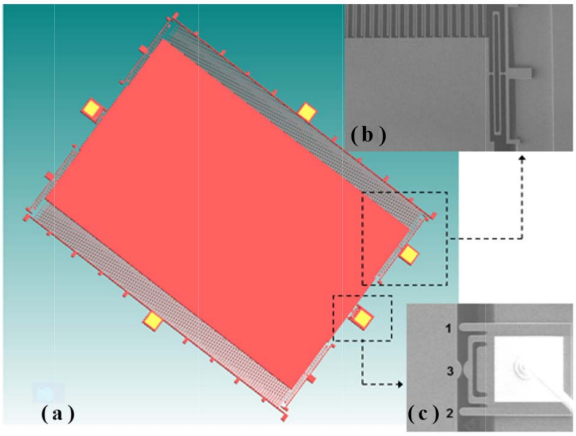

Fig. 1. (a) Device prototype showing beams and end-stop position with respect to proof mass. (b) and (c) are SEM images showing beams and electrodes to the top right, and end-stop to the bottom right.

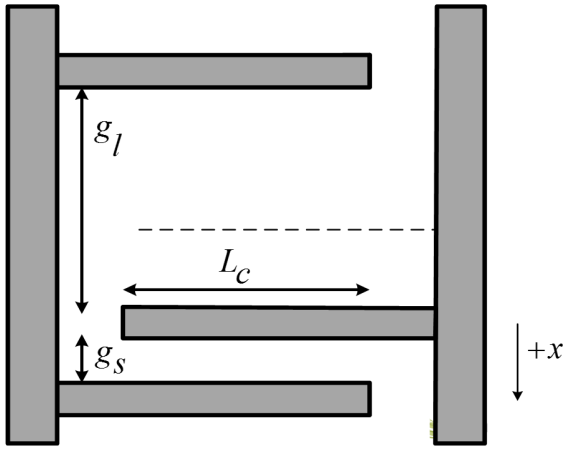

Fig. 2. Off-set geometry of electrodes and respective parameters.

in order to support design. Rather few studies have been carried out so far considering the nonlinearities due to impacts at end-stops for in-plane gap-closing micro energy harvesters, compared to what has been done for out-of-plane gap-closing devices [9], [13]. A prerequisite to model these effects is a sufficiently accurate model of the nonlinear dynamics up to the state of impacts.

In this paper, we present characterization, modeling and analysis of a nonlinear in-plane gap closing energy harvester with nonlinearities in fluid damping, a nonlinear electromechanical transducer, and impact nonlinearities at end-stops. The device is modeled such that fringing field effects are taken into account while defining the capacitances in the electrical subsystem of the lumped model. The nonlinear damping force and impact force are introduced in the model to capture the strong effect of mechanical nonlinearities on the behavior of the system. In contrast to [21], the damping force model is discussed in detail. Experiments and SPICE simulations are used to study the effect of nonlinearities on device response at different bias voltages and acceleration amplitudes.

The outline of this paper is as follows. Section II presents device design and the experimental setup used to characterize it. The measurement results under a set of different operating conditions are reported in Section III. Further, in section IV, the lumped modeling of the device, along with physical equations used to analyze device behavior, is discussed in detail. The measured and simulated behavior of the device are compared and discussed in Section V. Finally, Section VI concludes the paper.

II. Device Description and Experimental Setup

A. Device Description

The fabricated vibration energy harvester with wire bonding at gold contact pads is shown in Fig. 1. The device was fabricated in the SOIMUMPS foundry process [22] with device layer thickness (T_d) 25 μm and has a total active area of 4×5 mm^2. The deep reactive-ion release etch from the backside in this process has the advantage that it reduces the parasitic capacitance between the proof mass and substrate.

The device incorporates four springs, each near a corner of the movable proof mass, and two sets of fixed electrodes each with one electrical contact pad. The anchors to the beams and fixed electrodes were designed carefully following the design rules to have only a small area of overlap between the anchor and substrate, which helps further in reducing the stray capacitances, as shown in Fig. 1(a). Fig. 1(b) shows a Scanning Electron Microscope (SEM) image of the pair of electrodes constituting an in-plane gap closing transducer. Recent progress on fabrication of electrets on the sidewalls of the transducer fingers [23], [24] opens the possibility of operating such transducers in continuous mode with internal biasing. However, we have chosen to use an external bias for characterization of the harvester.

When excited, the proof mass motion modulates the capacitances between the fixed electrodes and the proof mass electrodes. Spring shaped mechanical end-stops are positioned such that the proof mass hits the end-stops at displacements $+/-$Z from the normal position.

The end-stop at position 3 in Fig. 1(c) is the primary end-stop, which is more compliant in nature than the relatively rigid secondary end-stops at positions 1 and 2. The secondary end-stops come into play when the proof mass goes beyond the displacement limit after impacting the primary end-stop at large excitation levels. Furthermore, there are small bumps designed on the fixed electrode fingers to avoid stiction between the movable and fixed electrode fingers in the fabrication process. Fig. 2 shows the gap-closing electrodes' off-set geometry with some design parameters defined. The off-set geometry of electrodes has been chosen as a key to future work where the electrodes can be charged/ discharged at their max/min capacitances utilizing the end-stops as mechanical switches. The end-stop is shown in Fig. 3. The energy harvester and end-stop dimensions are given in Table I and Table II, respectively.

B. Experimental Setup

A device under test is shown in Fig. 4, where it is mounted in a chip carrier which is glued on a printed circuit board with a buffer amplifier and load resistors. The device is covered

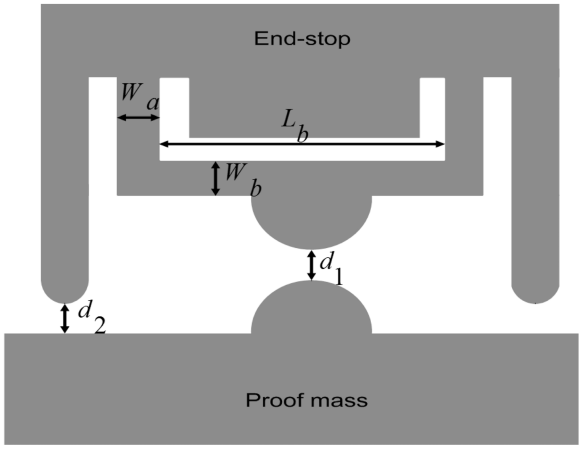

Fig. 3. End-stop geometry.

TABLE I
DIMENSIONS OF ENERGY HARVESTER

Parameters	Layout Values	Model Values
Active area	4 mm × 5 mm	
Device layer thickness, T_d	25 μm	
Length of spring	545 μm	
Width of spring	6.2 μm	
Overlap length of capacitor finger, L_C	335 μm	
Width of capacitor finger, W	6.20 μm	5.46 μm
Number of gaps between electrodes on each side of proof mass, N_g	226	
Gap between movable electrode and lower fixed electrode, g_s	7.50 μm	8.24 μm
Gap between movable electrode and upper fixed electrode, g_l	22.50 μm	23.24 μm
Displacement limit of movable electrodes, $\pm Z$	5.50 μm	6.24 μm

TABLE II
END-STOP DIMENSIONS

Parameters	Layout Values	Model Values
W_a	20 μm	
L_b	170 μm	
W_b	13 μm	
d_1	5.5 μm	6.24 μm
d_2	7 μm	

by a handmade plastic cap which does not provide perfect encapsulation but gives some protection from contamination like dust particles. The printed circuit board is further mounted

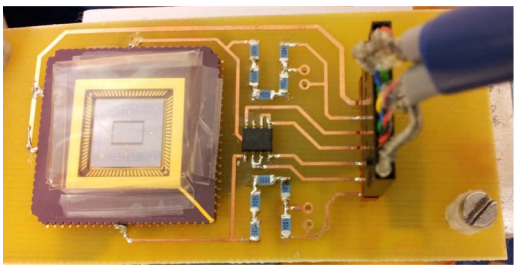

Fig. 4. A device under test with buffer amplifier and load resistors mounted on the printed circuit board.

TABLE III
BIAS VOLTAGE AND CORRESPONDING FREQUENCY

Bias Voltage (V)	0.5	3	5	8
Frequency (Hz)	730	724	712	629

on a TIRA shaker equipped with power amplifier, together with PCB Piezotronics Inc. (model 352A56A) accelerometer that measures the acceleration signal. The device is biased by an external voltage source connected to contact pads on the anchors of the fixed electrodes. The data from the input excitation signal and output voltage is analyzed and measured in parallel by a PC using National Instruments' LabView v9.0.1 and an NI-USB-6211 DAQ, which also logs the signal from the accelerometer.

In the experiments, the vibration frequency is swept at constant acceleration amplitude. Each output port is connected to a load resistor. The voltage across each resistor is measured through a buffer amplifier connected to the DAQ.

III. EXPERIMENTAL RESULTS

In this section, we present the measurements of the device under frequency sweeps at fixed acceleration amplitude (chirps). The bias voltage and the acceleration amplitude were varied in the experiments. The end-stops were kept at the same potential as the proof mass.

Table III shows the variation in the frequency peak with respect to bias voltage at a low input RMS acceleration of approximately 0.09 g and demonstrates the expected decrease in frequency due to the electromechanically lowered system stiffness.

We measured the frequency response of the harvester on increasing the excitation levels at a particular bias voltage. The experimental data in all the experiments was collected for 40 s with sample rate of 48×10^3 Hz.

Fig. 5 shows the experimental results for frequency up- sweep and down- sweep at 5-V bias and for different RMS accelerations approaching the linear regime of device behavior at the low end of the acceleration range. The frequency was swept up- and down- between 690 Hz–750 Hz and 750 Hz–660 Hz in 40 s + 40 s at 0.1 g and 0.5 g acceleration amplitude, respectively. Spring softening with increase in excitation level is clearly seen as the peak frequency drifts

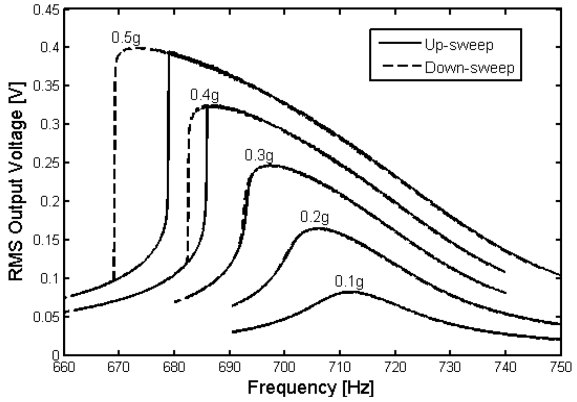

Fig. 5. Measurement of output voltage for frequency up- sweep and down- sweep at bias voltage of 5 V and various RMS accelerations.

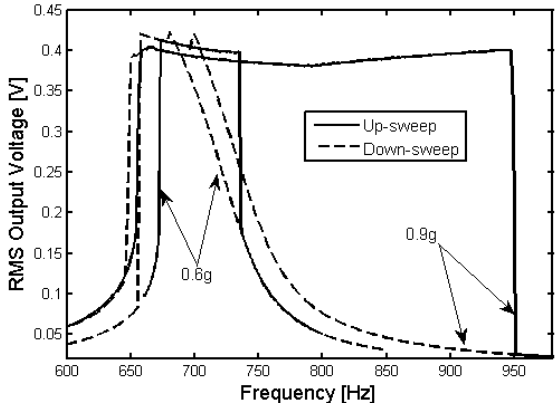

Fig. 6. Measurement for frequency up- sweep and down- sweep at 5-V bias with RMS acceleration 0.6 g and 0.9 g.

downwards and develops a hysteresis between the up- and down- sweeps. The spring softening behavior is due to electrostatic forces in the transducers as one could expect in this type of transducer design [14]. This mechanism can be used as an alternative to incorporating softening beams in the device design [17].

At sufficient acceleration amplitude, the proof mass motion is limited by the end-stops and the output voltage saturates, the example with 5-V bias is shown in Fig. 6. The frequency sweeps in Fig. 6 show the multivalued response of the harvester thereby increasing the up- and down- sweep bandwidth of the harvester with increasing excitation. This multivalued response can be utilized when the vibration frequency changes over time as it widens up the bandwidth of the harvester [10]. The hysteresis on the high-frequency side of the response is typical of harvesters with impacts and other abrupt increases in stiffness [3], [10], [13], [25]. There is also hysteresis on the low-frequency side where the hysteresis was already seen in Fig. 5. The 3-dB bandwidth at RMS acceleration 0.1 g is 19.6 Hz and increases to 293 Hz for frequency up-sweep at RMS acceleration 0.9 g. Table IV compares measured normalized up-sweep frequency bandwidth, NFB, defined as the -3 dB bandwidth divided by the central frequency of 3-dB band, for some wideband MEMS energy harvesters.

TABLE IV
COMPARISON OF MEASURED NORMALIZED UP-SWEEP FREQUENCY BANDWIDTH

Reference	Approach	RMS Acceleration A (g)	NFB
[3]	End-stops	0.34	0.18
[13]	End-stops	0.7	0.13
[25]	End-stops	2.70	0.22
[26]	End-stops	1.4	0.42
[27]	Amplitude limitation mechanism	1.0	0.47
[28]	Nonlinear spring	1.0	0.62
[29]	Nonlinear spring	$4 \cdot 10^{-3}$ g^2/Hz (white noise vibration)	0.98
This paper	End-stops	0.9	0.37

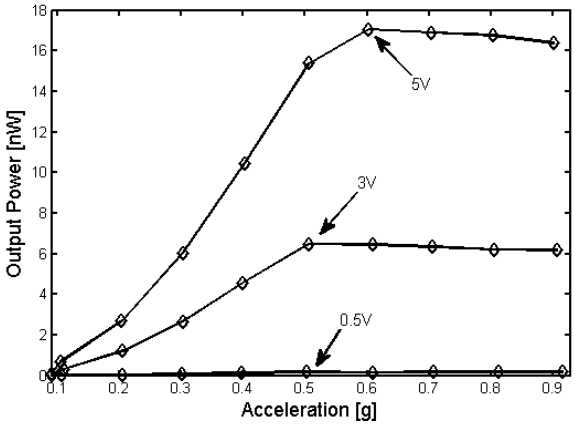

Fig. 7. Maximum measured output power for frequency up-sweep at different RMS accelerations for various bias voltages 0.5 V, 3 V, and 5 V.

Fig. 7 shows the maximum measured output power at different RMS input accelerations and different operating bias voltages for frequency up-sweep at load resistance 20 MΩ. At a fixed acceleration, the output power increases approximately quadratically with bias voltage. For example, at RMS acceleration 0.5 g, output powers at 0.5-V, 3-V and, 5-V bias are 0.16 nW, 6.48 nW, and 15.40 nW, respectively. The impact of the proof mass at the end-stop limits the modulation of capacitance, which then reaches its maximum and hence saturates the output power. When impacting, the device behaves nonlinearly resulting in jump phenomena in the frequency response. This phenomenon strongly depends on the parameters of the end-stop as discussed in detail in sections IV and V. The proof mass hits the end-stops at RMS acceleration below 0.5 g for 0.5-V and 3-V bias, and above 0.5 g for 5-V bias. This increase in acceleration threshold

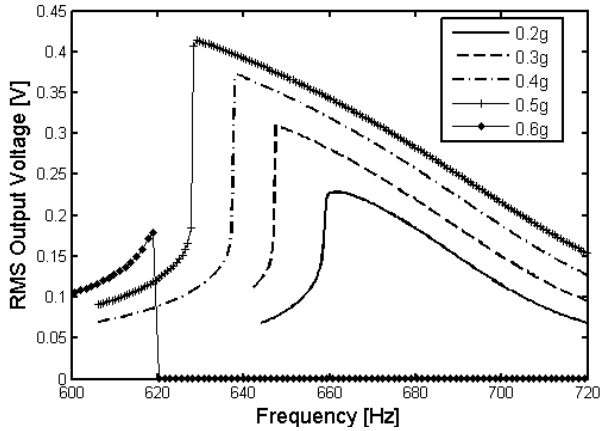

Fig. 8. Up- sweep frequency response at 8-V bias and with different RMS acceleration showing the spring softening and dynamic pull-in behavior.

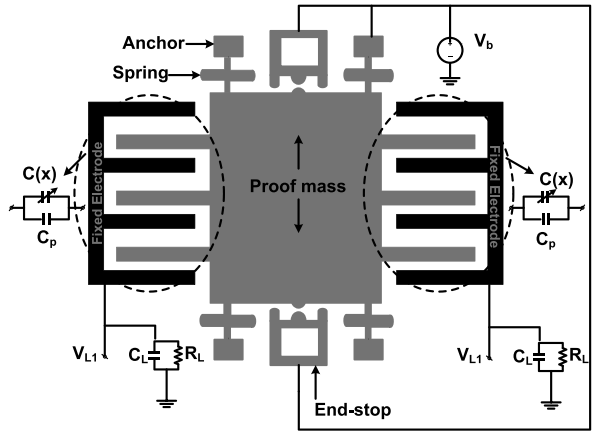

Fig. 9. Schematic drawing of comb-drive electrostatic energy harvester.

values could be because of the change in electrical damping in the system with increase in bias voltage.

Dynamic pull-in is observed at 8-V bias and 0.6 g, Fig. 8, while the static pull-in for the device is around 16 V. Dynamic pull-in takes place when the proof mass, at sufficient bias and strong enough acceleration amplitude, crosses an intermediate potential barrier [12], [30] and impacts with the end-stop. If the proof mass has sufficiently low kinetic energy after the impact, it becomes trapped at a potential minimum at the end-stop. The spring softening is observed as the input RMS acceleration is increased, and at 0.6 g, the proof mass is pulled in. However, no pull-in is observed around this acceleration level for 0.5 V, 3 V and 5 V. Therefore, for each acceleration amplitude there is an optimal value of bias voltage.

IV. Modeling and Analysis

To analyze the behavior of the energy harvester, an equivalent-circuit lumped-model was developed. In this section, we discuss the model and will compare the simulation results to experimental results in the next section. Fig. 9 shows the schematic drawing of the comb-drive energy harvester.

A. Capacitance Correction

The variable capacitance between the movable set of proof mass electrodes and the fixed electrodes on one side of the

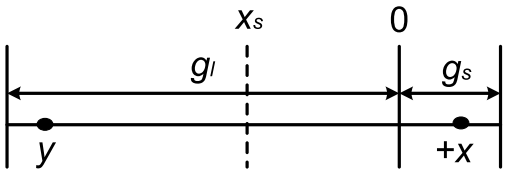

Fig. 10. Geometry of a pair of electrodes.

proof mass, excluding capacitances due to fringing fields, is

$$C(x) = \frac{C_0}{\left(1 + \frac{x}{g_l}\right)\left(1 - \frac{x}{g_s}\right)} \tag{1}$$

where x is displacement of the proof mass,

$$C_0 = \frac{N_g L_c T_d \varepsilon_0}{2}\left(\frac{1}{g_l} + \frac{1}{g_s}\right) \tag{2}$$

and ε_0 is the vacuum permittivity.

It is important to have a sufficiently accurate capacitance model of the transducer in order to get a reasonable agreement between the model and experiment. One of the factors effecting the overall capacitance is the capacitance due to fringing fields. Taking into account the fringing fields increases the total capacitance of the device [31]. In order to include fringing fields in the model, a finite element method (FEM) analysis of the capacitance variation was made and the result fitted to the form

$$C(x) = \frac{A(x)}{\left(1 + \frac{x}{g_l}\right)\left(1 - \frac{x}{g_s}\right)} \tag{3}$$

where $A(x)$ is a suitable, well behaved function.

We chose a second order polynomial $A(x) = A_0 + A_1 x + A_2 x^2$, where the coefficients, A_0, A_1, A_2 are obtained from the fit and are not all independent. With the equilibrium displacement of the proof mass at zero bias defined as $x = 0$ because of the asymmetry in the equilibrium position indicated in Fig. 2, the middle position for a movable electrode finger is $x_s = -(g_l - g_s)/2$ as indicated in Fig. 10. The capacitance should be symmetric with respect to displacement about x_s i.e. the displacement $y = 2x_s - x$ should give the same capacitance as x. Thus, requiring $A(x) = A(y)$, we find the constraint

$$A_1 + 2A_2 x_s = 0 \tag{4}$$

By taking (4) into account, (3) can be written in the form

$$C(x) = C_f + \frac{C_0}{\left(1 + \frac{x}{g_l}\right)\left(1 - \frac{x}{g_s}\right)} \tag{5}$$

with

$$C_0 = A_0 - C_f \quad \text{and} \quad C_f = -A_2 g_s g_l \tag{6}$$

From (5) it is then clear that the displacement dependence of the parallel plate form (1) can capture some fringing field effects by addition of a constant parallel capacitance C_f and modification of the value of the nominal capacitance C_0. The variations in capacitance with the position of proof mass from (1) and (5) are compared in Fig. 11. The difference between the simple analytical form (1) and the FEM result

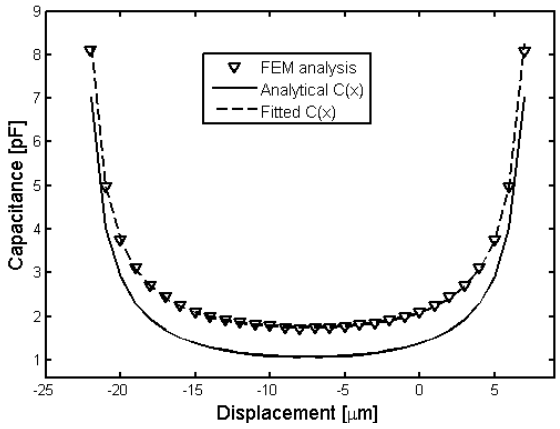

Fig. 11. Comparison between capacitance models.

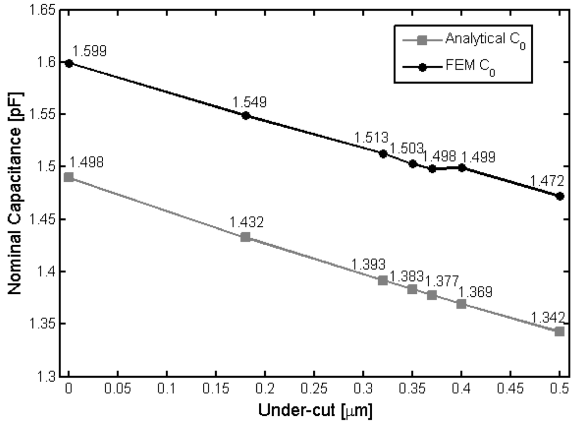

Fig. 12. Nominal capacitance versus under-cut.

is significant, and the fitted form (3) captures the FEM result accurately.

The under-cut in the etch process, i.e. the lateral extension of the etch under the mask, can be important for the effectiveness of the harvester [20]. The under-cut may result in variability of the air gap between the electrodes [32]. The possible deviation from nominal gap needs to be accounted for by fits to the measurement or other means. In this paper, the under-cut is treated as uniform throughout the thickness of the device layer for simplicity. Thus, the air gap between the electrodes increases from the mask dimension by twice the under-cut value. In order to avoid introducing unwarranted degrees of freedom in such a parameter fit, the under-cut dependence of C_f and C_0 must be determined.

Fig. 12 shows the nominal capacitance C_0 from (2) and (6) for seven different cases of under-cut i.e. 0 μm, 0.18 μm, 0.32 μm, 0.35 μm, 0.37 μm, 0.4 μm and 0.5 μm and can be used for this purpose. The capacitance C_0 turned out to be almost constant, varying less than 3.2% over this range. Hence, the combination of FEM and a fit to (3) provide a capacitance model whose parameters can be calculated if all dimensions are known.

In addition to the capacitances that are internal to the transducer finger-structure, we expect capacitances from electrodes to the frame and package which we model as a parasitic capacitance C_p added in parallel to the variable capacitance. Thus, the total transducer capacitance using (5) can be written as

$$C^A(x) = C_p + C_f + \frac{C_0}{\left(1+\frac{x}{g_l}\right)\left(1-\frac{x}{g_s}\right)} \tag{7}$$

The parameter C_f merely contributes a constant capacitance in addition to C_p. Therefore, if C_p is obtained from fit to experiments, one can in practice set $C_f = 0$ and consider it accounted for in the fitted value for C_p. Thus, (7) becomes

$$C^A(x) = C_p + \frac{C_0}{\left(1+\frac{x}{g_l}\right)\left(1-\frac{x}{g_s}\right)} \tag{8}$$

where C_p is a fitted parameter and C_0 comes from the FEM analysis in Fig. 12. This procedure to determine the total internal capacitance, where C_p and C_0 to a certain extent account for fringing capacitances, also applies to overlap-varying transducers [7] and to complex harvester designs [25]. In [7], C_0 in the lumped model was fitted freely to achieve agreement between experimental and simulated data, while the under-cut is treated as a free parameter in this study and C_0 is analyzed for a range of under-cut values, fig. 12.

In conclusion, the second-order fit for A(x) used here retains the simple form of (8) while securing accuracy as shown in Fig. 11. A more complicated fitting function would complicate the model while only providing a modest potential for improved accuracy.

B. Squeeze-Film Damping Force

In addition, squeeze-film damping force is an essential feature of energy harvesters, which can be linear or nonlinear depending on the geometry of the device. Usually, a phenomenological linear damping with a coefficient b taken from experiments is used in equivalent circuit modeling. At small acceleration amplitudes, damping can be modeled by a linear damper but at higher acceleration amplitudes, nonlinearity can no longer be ignored. In this device, the different spacing between the capacitor fingers gives different gas damping contributions with some squeeze effects on the two sides of each moving finger. The damping in the smaller gaps with nominal size g_s dominates over damping in the larger gaps with nominal size g_l. For the smaller gaps, we expect the damping to be well described by the theory of squeeze-film damping, in particular when the gap is near its minimum and the damping is of large magnitude. For the larger gaps, each gap is of the same order of magnitude as the finger width and the enclosed air can hardly be characterized as a film. We therefore model only the smaller gaps as squeeze-film dampers and treat all other damping mechanisms as a resultant phenomenological linear damper. The squeeze number for smaller gaps g_s is $\sigma = 12\mu T_d^2\omega/P_a g_s^2 = 2.9\cdot 10^{-5}$, where μ is the viscosity of air at room temperature, ω is the angular frequency and P_a is ambient pressure. This shows that the flow is incompressible and hence the air-spring effect is negligible [33]. The damping model is then

$$F_d = \left(2b_{\text{squeeze-film}}(x) + b_1\right)\dot{x} \tag{9}$$

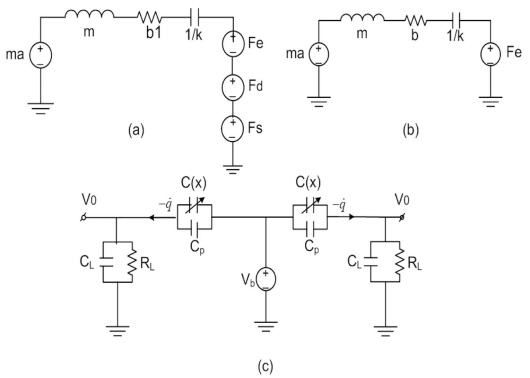

Fig. 13. (a) Equivalent circuit for mechanical subsystem with nonlinear damping force and impact force (b) Equivalent circuit for mechanical subsystem with linear damping force (c) Electrical circuit.

with

$$b_{\text{squeeze-film}} = \frac{N_g \mu L_c T_d^3}{2(g_s - x)^3}. \tag{10}$$

b_1 characterizes the phenomenological linear damping, which is obtained by fitting simulated frequency response to the measurement results. The squeeze-film part is obtained from [33]. The nonlinear effect of the squeeze-film damping force is further discussed in section V on comparing simulation results to experimental results.

C. Impact Force

The displacement of the proof mass is limited by the end-stops in the device as shown in Fig. 3. For sufficient acceleration amplitude, the proof mass frequently hits the end-stops which are modeled as spring dashpot systems. The end-stops add to nonlinearities in the motion of the proof mass which in turn depend on the strength of the impacting force between the proof mass and the end-stops. The impact force F_S at the end-stop is defined as

$$F_S = k_S \Delta x + b_S \Delta \dot{x} \tag{11}$$

where k_S is the stiffness of the end-stops, Δx is the displacement of the end-stops on impact with the proof mass, and b_S is the damping coefficient for the end-stops.

Thus, the electrostatic force from the two identical transducers and Newton's second law for the proof mass are respectively given by

$$F_e = q^2 \frac{d}{dx}\left(\frac{1}{C^A(x)}\right) \tag{12}$$

and

$$m\ddot{x} + kx + F_e + F_s + F_d = ma \tag{13}$$

where q is the charge on each of the variable transducers with total capacitance $C^A(x)$.

Fig. 13(a) shows a mechanical subsystem with impact force F_s, linear damping constant b_1 and nonlinear damping force F_d, while Fig. 13(b) shows a mechanical subsystem of the device with linear damping force with constant b.

TABLE V
MODEL PARAMETERS OF THE HARVESTER

Parameters	Values
Proof mass, m	0.92 mg
Device stiffness, k	19.42 N/m
Damping constant, b	$9.48 \cdot 10^{-5}$ Ns/m
b_1	$5.50 \cdot 10^{-5}$ Ns/m
Nominal capacitance, C_0	1.49 pF
Parasitic capacitance, C_p	5.5 pF
Load resistance, R_L	20 MΩ
Load capacitance, C_L	2 pF

For both models, the fictitious force ma experienced due to the acceleration a of the device frame excites the mass m, which is suspended in a spring with stiffness k and, is subject to an electrostatic force F_e from the transducers.

As shown in Fig. 13(c), the transducer is biased by an external voltage source V_b connected to the variable capacitance $C(x)$ and a load consisting of a resistance R_L and capacitance C_L. It is an arbitrary choice treating the two sides as two separate transducers here. Since the parameters are the same, they could have been lumped into one. The output voltage V_0 of a transducer is

$$V_0 = \frac{q}{C^A(x)} + V_b \tag{14}$$

V. COMPARISON BETWEEN MEASURED AND SIMULATED RESPONSE

The lumped model in Fig. 13 with capacitance correction using (8) is simulated for linear and nonlinear squeeze-film damping force and the results are compared to experiments. Since both the nonlinear damping force from (9) and C_0 from (6) are gap dependent, these two values are constrained and have the under-cut value discussed in section IV as the only free parameter. The best under-cut value was determined by SPICE simulations over the range of values used in Fig. 12. We found that 0.37 μm gave the best agreement between simulations and experimental data. The model parameters for fits with linear and nonlinear squeeze-film damping are shown in Table V. The damping coefficient b in the linear model is obtained from experimental data at small bias 0.5 V and small RMS acceleration amplitude 0.09 g. C_p is obtained by fitting simulated response to the measured frequency response. C_0 is obtained from (6). R_L is the resistor component value. It was chosen based on preliminary simulations prior to the parameter fit. The proof mass m was calculated from the layout and $k = m\omega_0^2$ was obtained from the peak of the measured frequency response in the linear regime.

Fig. 14 shows experimental data together with SPICE simulations for linear and non-linear damping force for three different RMS acceleration amplitudes at 5-V bias. Thus, taking into account the nonlinearity in squeeze-film damping force between the electrodes with smaller gaps g_s, the SPICE simulation result falls quite close to experimental output.

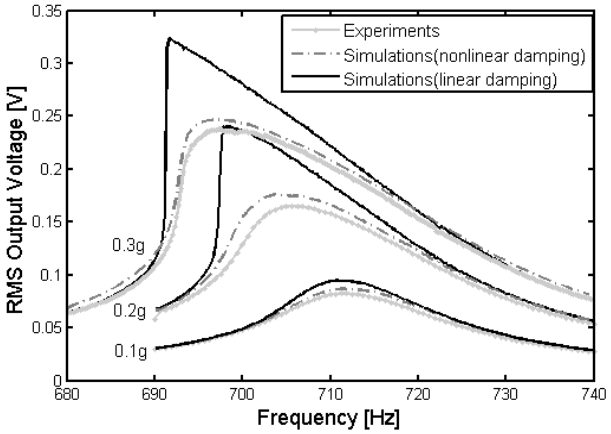

Fig. 14. Up- sweep frequency response at 5-V bias with RMS acceleration 0.1 g, 0.2 g, and 0.3 g.

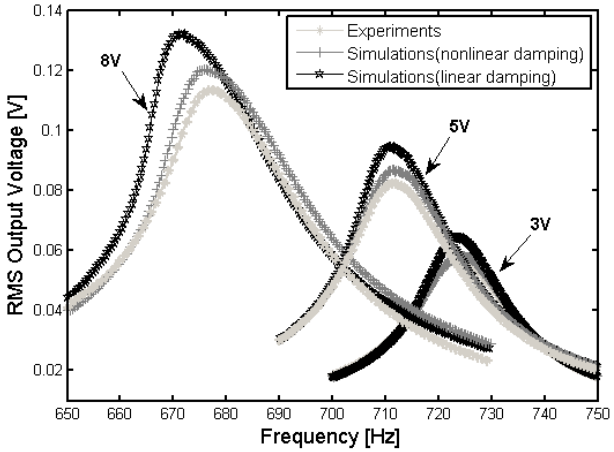

Fig. 15. Up- sweep frequency response at 3-V, 5-V, and 8-V bias with RMS acceleration 0.1 g.

As seen in Fig. 14, the linear damping model predicts the jump phenomena at low accelerations where neither the experiments nor the nonlinear damping model exhibits this phenomenon. A clearer distinction between the experiments and simulations for linear damping model is seen at higher acceleration amplitudes for given bias.

Linearization of (10) around $x = 0$ gives a damping coefficient $2b_{\text{squeeze-film}} = 3.80 \cdot 10^{-5}$Ns/m. Subtracting this contribution from the linear damping coefficient in the linear damping model gives $b - 2b_{\text{squeeze-film}} = 5.68 \cdot 10^{-5}$Ns/m which compares favorably with the fitted value $b_1 = 5.50 \cdot 10^{-5}$Ns/m for (9) and shows that the two models are consistent for small displacement and small biases as they should.

Along with the squeeze-film damping in the finger structure, the motion of the proof mass will create gas flow on top and bottom of it. This motion results in slide film damping on the top and the bottom of the proof mass. Since the proof mass is far away from any external object above and below it, this damping force is of Stokes flow type. The damping coefficient is $b_{\text{slide-film}} = 2\mu A/\delta$, where $\delta = \sqrt{\frac{2\mu}{\rho\omega}}$, ω is the angular frequency of the moving plate, ρ is the density of air and A is the area of the moving plate [34]. We find $b_{\text{slide-film}} = 0.70 \cdot 10^{-5}$Ns/m which accounts for 13% of b_1. The remaining contributions can be due to the complex gas flow in other parts of the structure; such as in larger gaps g_l of the finger structure and in the spring/end-stop structures.

The squeeze-film contribution is 41% of the total linearized damping coefficient. Therefore, squeeze-film damping in the smaller gaps g_s has a significant contribution to the total damping of the device already at small displacements and becomes dominant when the gap between the moving electrodes decreases due to the motion of the proof mass.

In the presence of the linear damping, a theoretical upper bound on output power is given by $P_{\text{bound}}/P_c \approx 2A/A_{\text{c}} - 1$ for $A > A_{\text{c}}$, $P_{\text{c}} = m^2A_{\text{c}}^2/8b_1$ and $A_{\text{c}} = 2b_1\omega Z/m$. The theoretical output power bound holds independently of transducer nonlinearities [35]. For an acceleration amplitude $A = \sqrt{2} \cdot 0.6g$ at 5-V bias, we find that $P_{\text{bound}} = 4.4P_{\text{c}}$ while the measured power is $P_{\text{measured}} = 0.92P_{\text{c}}$. The theoretical bound does not take in account nonlinear squeeze-film damping, hence comes out to substantially higher than measured power. The measurement is for a non-optimized load resistance of $20M\Omega$. We checked the load-dependence at 5-V bias and RMS acceleration amplitude 0.6 g by SPICE simulation. By varying the load from 5 $M\Omega$ to 90 $M\Omega$, we estimated that the non-optimum loading reduces the power by merely 1%.

TABLE VI
END-STOP PARAMETERS

Parameters	Values
End-stop stiffness, k_{S}	$3.9{\cdot}10^4$ N/m
Displacement limit,+/- Z	+/- 6.24um

The shifting in the frequency peak on increasing the electrical damping at RMS acceleration 0.1 g is shown in Fig. 15. The shift in the peak frequency to lower frequencies on increasing the bias shows the dependence of the harvester output on bias voltage. With the linear damping model, the RMS output voltage comes out to be higher than in the experiments. The discrepancy increases with increasing bias at given acceleration amplitude. The misfit between the experiments and simulations on increasing the bias voltage is obvious as the spring softening behavior is more prominent at higher voltages.

Fig. 14 and Fig. 15 show that the effect of nonlinear squeeze-film damping not only increases on increasing the acceleration amplitude at fixed bias but also increases on increasing the bias voltage at fixed acceleration amplitude. Thus, the nonlinear squeeze-film damping has a profound effect on the dynamics and is absolutely necessary in order to capture the observed behavior.

The effects of nonlinearities at end-stops are investigated with model parameters as stated in Table VI. The under-cut of the mask in the microfabrication process is taken into

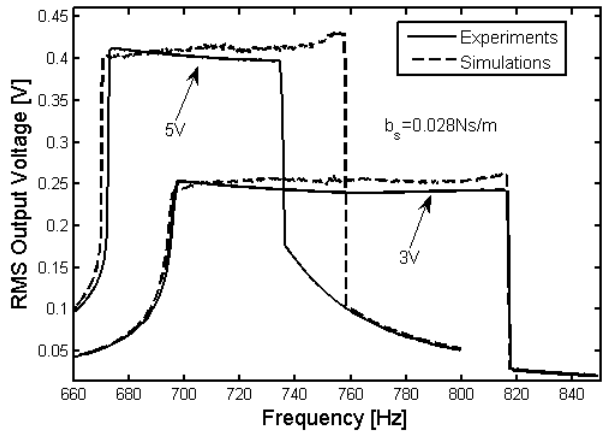

Fig. 16. Up- sweep frequency response at 3-V and 5-V bias with RMS acceleration 0.6 g.

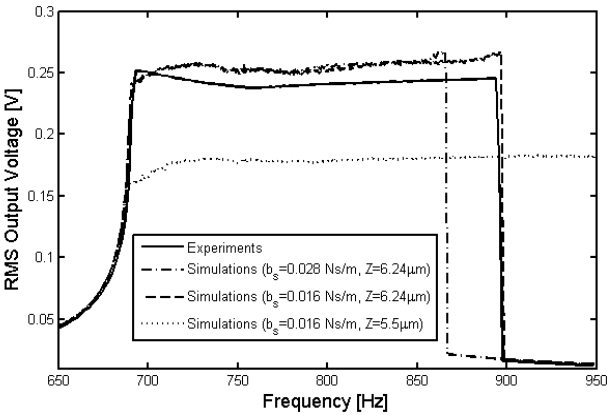

Fig. 17. Up- sweep frequency response at 3-V bias with RMS acceleration 0.7 g.

account when defining the displacement limit of the proof mass. The value from the previous parameter fit was used. The end-stop stiffness is obtained from a FEM analysis of the end-stop's displacement when the applied force is varied. The damping coefficient in the end-stops b_s is fitted. It turns out to be bias and acceleration-amplitude dependent.

Fig. 16 shows the experimental data and SPICE simulations for biases 3 V and 5 V, and RMS input acceleration 0.6 g. The damping coefficient b_s is fitted for 3-V bias at 0.6 g. With this value, it does not fit well for 5-V bias at 0.6 g, in that the jump-down frequency differs significantly from the experiment. However, deviation in the jump-up frequency is negligibly small.

Fig. 17 compares the experimental data and SPICE simulation for 3-V bias and RMS acceleration 0.7 g. The result is investigated for two different values of b_s; one is obtained from the previous parameter fit at 3-V bias and 0.6 g while the other is obtained from a parameter fit at 3-V bias and 0.7 g. The effect of displacement limit Z on jump frequencies at fixed b_s is also captured in Fig. 17. Thus, the fitted damping coefficient changes with changing acceleration level at same bias voltage. Decreasing the damping coefficient increases the jump-down frequency and thus gives better fit [3].

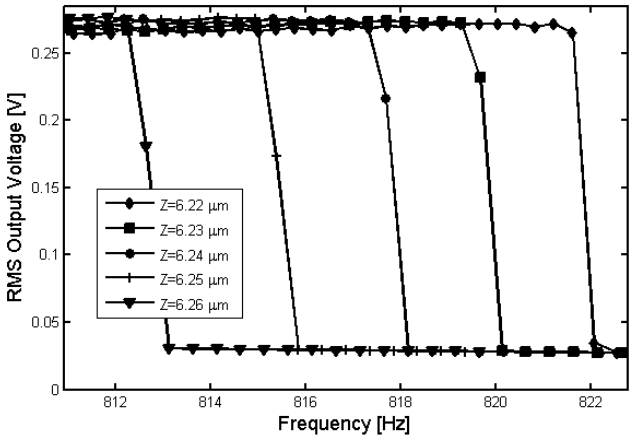

Fig. 18. Up- sweep frequency response at 3-V bias with RMS acceleration 0.6 g.

In addition, the jump frequencies vary with varying the distance between the proof mass and the end-stop. The sweeps in Fig. 17 show that the proof-mass impacts with the end-stop take place for a wider range of frequencies when the displacement limit Z is smaller. The jump-down frequency for smaller Z lies beyond the up-sweep frequency range, as shown in Fig. 17. The same phenomena has been observed in [3] with a mechanical end-stop only on one side of the piezoelectric energy harvester.

The comparisons between simulations and measurement in Fig. 16 and Fig. 17 show difficulties in replicating the jump-down frequencies in different situations with one parameter set. The jump-down frequency depends on the degree of nonlinearity and damping of the system [36]. The nonlinearity and damping in turn largely depend on the end-stop parameters and state of the system before impact occurs. The under-cut in the etched structure is taken into account in these simulations and decides the displacement at which the end-stops are impacted. It is possible that this value is slightly different for the end-stop structures than for the finger patterns due to the difference in etch openings. The discrepancy in under-cut will surely influence the displacement waveform of the proof mass and could possibly affect the stability of the high-amplitude orbit. A further factor could be asymmetries in the displacement range due to process variations, such as irregularities in the etched sidewalls being different for the two end-stop structures.

It should be noted that the jump-down frequency is extremely sensitive to fine details in the model. The simulations for a sensitivity check at fixed bias and RMS acceleration amplitude gave more than 8Hz change in jump-down frequency for a 40 nm change in end-stop position between Z=6.22 μm and 6.26 μm, fig. 18. Also, the change in jump-down frequency was approximately 5 Hz for 0.004 Ns/m change in b_S between 0.026 Ns/m - 0.03Ns/m and 3 Hz for 0.4 N/m change in k_S between 3.7 N/m - 4.1 N/m, respectively.

Finally, it is possible that the impacting force F_S which governs the behavior of the end-stop is not well captured by the spring-damper model as this design has considerably more

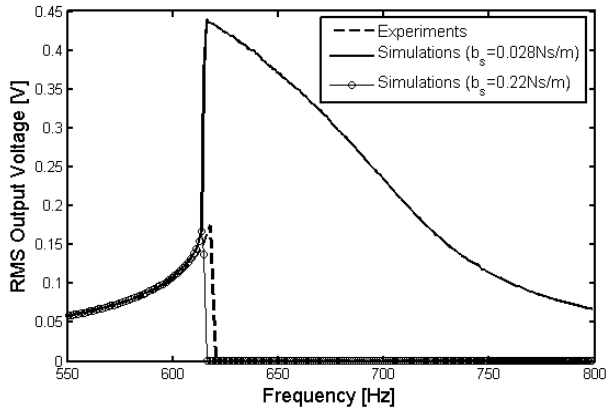

Fig. 19. Up- sweep frequency response at 8-V bias with RMS acceleration 0.6 g.

compliant end-stops than in previous designs where this model has proved successful [3]. The big difference in optimal end-stop damping between fits at different acceleration amplitudes, supports this hypothesis. A possible mechanism that could make the end-stop model differ from a spring-damper system is stiction forces between the proof mass and the end-stop, and the damping in the end-stop structure.

The dynamic pull-in behavior at 8 V and RMS acceleration 0.6 g was investigated with the end-stop model and is compared to the measurements in Fig. 19. It is observed that with $b_S = 0.028$ Ns/m obtained from the previous parameter fit at 3-V bias and RMS acceleration 0.6 g, the electromechanical softening behavior causes a jump-up instead of pull-in. The observation can be interpreted as the frequency being swept into the range where only a single orbit exists or as the perturbation of the impact itself being enough to initiate a change of orbit. If the end-stop damping coefficient in the model is increased to at least $b_S = 0.22$ Ns/m, a dynamic pull-in behavior that fits well with experiments is found.

The dynamic pull-in behavior is something we would normally rather avoid in the harvester. The type of analysis carried out here can be helpful in design by predicting when pull-in takes place. However, there are challenges with respect to how accurate predictions can be made because the local minimum at the end-stop is a consequence of two opposing forces, the spring force and the electrostatic force, and the precise displacement at which end-stops are engaged. The latter is more sensitive to process variations than the capacitance because it depends on the precise details of the etched surfaces while these details are lumped together in the total capacitance.

Thus, we observe that the end-stop damping needed some adjustment to achieve agreement with observations. Hence, it is an interesting topic for future work how to capture the whole range of operating conditions with a fixed parameter set.

VI. Conclusion

We have experimentally characterized a vibration-driven in-plane gap closing electrostatic energy harvester fabricated in SOIMUMPS foundry process displaying rich nonlinear behavior. An electrical equivalent-circuit model based on a combination of measured geometrical dimensions and fitted parameters was simulated and the results compared to experiments. The fringing field effect on the transducer capacitance studied by finite element method was taken into account in defining the capacitance in the model. The proof mass was calculated from the layout, while spring stiffness, linear damping, parasitic and load capacitances were obtained by fitting the simulated response to measured response of the harvester. In addition, the dominating stray effects on the variable part of the transducer capacitance were accounted for using only the deviation of gap width due to the etch process. The best value for gap width was chosen by fitting the simulated and measured frequency response. This gap width also entered the calculations of squeeze-film damping.

The nonlinear squeeze-film damping in the capacitor fingers with off-set geometry results in a model with predictions close to experimental results, and is investigated to a level of detail that has been lacking in other experimental electrostatic harvester studies with nonlinear squeeze-film damping. An established formula for large gap variations was used in the model while the remaining damping was treated as a phenomenological linear damper with a fitted parameter. The equivalent circuit model was compared for nonlinear squeeze-film and linear damping, where the linear damping coefficient was obtained from fits between the experimental data and SPICE simulations. Our comparison showed that nonlinear squeeze-film damping is essential to capture the device behavior; without this effect, the model predicts jump phenomena at significantly smaller accelerations than what is the case in the experiments and predicts higher RMS output voltages.

Modeling for large-amplitude accelerations showed that a simple spring-damper model for the end-stops gives a good account of the main features of the device response with an adjustment on the end-stop damping coefficient. For the jump-down frequency, the present model can only be made accurate at a specific acceleration and bias voltage. There were challenges in predicting accurately the condition of dynamic pull-in at 8 V and RMS acceleration 0.6 g with fixed parameter set, even though the model does predict the phenomena on adjusting the end-stop damping.

The usefulness of the model as a tool for performance prediction in design, as opposed to analysis after fabrication, mostly hinges on the ability to predict the parameters of the model. These model parameters can be obtained by a combination of process characterization and numerical computation as described in this paper. The most problematic part is the jump-down frequency at large acceleration which can not be accurately predicted without further improvements in the end-stop modeling. Nevertheless, the results obtained with the present model show that other features of the device responses are accounted for with high fidelity.

In conclusion, a model is well established to account for the simultaneous presence of three significant nonlinear effects that are crucial to the dynamics of the device: nonlinear squeeze-film damping, nonlinear system stiffness due to electromechanical coupling and impacts with end-stops.

REFERENCES

[1] X. Cao, W.-J. Chiang, Y.-C. King, and Y.-K. Lee, "Electromagnetic energy harvesting circuit with feedforward and feedback DC–DC PWM boost converter for vibration power generator system," *IEEE Trans. Power Electron.*, vol. 22, no. 2, pp. 679–685, Mar. 2007.

[2] P. Glynne-Jones, M. J. Tudor, S. P. Beeby, and N. M. White, "An electromagnetic, vibration-powered generator for intelligent sensor systems," *Sens. Actuators A, Phys.*, vol. 110, nos. 1–3, pp. 344–349, Feb. 2004.

[3] L.-C. J. Blystad and E. Halvorsen, "A piezoelectric energy harvester with a mechanical end stop on one side," *Microsyst. Technol.*, vol. 17, no. 4, pp. 505–511, Apr. 2011.

[4] P. D. Mitcheson, E. M. Yeatman, G. K. Rao, A. S. Holmes, and T. C. Green, "Energy harvesting from human and machine motion for wireless electronic devices," *Proc. IEEE*, vol. 96, no. 9, pp. 1457–1486, Sep. 2008.

[5] L.-C. J. Blystad, E. Halvorsen, and S. Husa, "Piezoelectric MEMS energy harvesting systems driven by harmonic and random vibrations," *IEEE Trans. Ultrason., Ferroelectr., Freq. Control*, vol. 57, no. 4, pp. 908–919, Apr. 2010.

[6] P. Miao, P. D. Mitcheson, A. S. Holmes, E. M. Yeatman, T. C. Green, and B. H. Stark, "MEMS inertial power generators for biomedical applications," *Microsyst. Technol.*, vol. 12, pp. 1079–1083, Sep. 2006.

[7] L. G. W. Tvedt, D. S. Nguyen, and E. Halvorsen, "Nonlinear behavior of an electrostatic energy harvester under wide- and narrowband excitation," *J. Microelectromech. Syst.*, vol. 19, no. 2, pp. 305–316, Apr. 2010.

[8] F. Cottone, P. Basset, R. Guillemet, D. Galayko, F. Marty, and T. Bourouina, "Non-linear MEMS electrostatic kinetic energy harvester with a tunable multistable potential for stochastic vibrations," in *Proc. IEEE 17th Int. Conf. Transducers Eurosensors*, Barcelona, Spain, Jun. 2013, pp. 1336–1339.

[9] R. Guillemet, P. Basset, D. Galayko, F. Cottone, F. Marty, and T. Bourouina, "Wideband MEMS electrostatic vibration energy harvesters based on gap-closing interdigited combs with a trapezoidal cross section," in *Proc. IEEE 26th MEMS*, Jan. 2013, pp. 817–820.

[10] M. S. M. Soliman, E. M. Abdel-Rahman, E. F. El-Saadany, and R. R. Mansour, "A wideband vibration-based energy harvester," *J. Micromech. Microeng.*, vol. 18, no. 11, p. 115021, Oct. 2008.

[11] G. De Pasquale, E. Brusa, and A. Soma, "Capacitive vibration energy harvesting with resonance tuning," in *Proc. DTIP MEMS MOEM*, Apr. 2009, pp. 280–285.

[12] R. Guillemet, P. Basset, D. Galayko, and T. Bourouina, "Design optimization of an out-of-plane gap-closing electrostatic vibration energy harvester (VEH) with a limitation on the output voltage," *Analog Integr. Circuits Signal Process.*, vol. 7, no. 1, pp. 39–47, Jul. 2011.

[13] P. Basset *et al.*, "Electrostatic vibration energy harvester with combined effect of electrical nonlinearities and mechanical impact," *J. Micromech. Microeng.*, vol. 24, no. 3, p. 035001, Feb. 2014.

[14] D. Hoffmann, B. Folkmer, and Y. Manoli, "Analysis and characterization of triangular electrode structures for electrostatic energy harvesting," *J. Micromech. Microeng.*, vol. 21, no. 10, p. 104002, Jun. 2011.

[15] Q. Fu and Y. Suzuki, "Large-dynamic-range MEMS electret energy harvester with combined gap-closing/overlapping-area-change electrodes," *J. Phys.: Conf. Ser.*, vol. 476, p. 012112, 2013.

[16] B. Yang, C. Lee, R. K. Kotlanka, J. Xie, and S. P. Lim, "A MEMS rotary comb mechanism for harvesting the kinetic energy of planar vibrations," *J. Micromech. Microeng.*, vol. 20, no. 6, p. 065017, Apr. 2010.

[17] D. S. Nguyen, E. Halvorsen, G. U. Jensen, and A. Vogl, "Fabrication and characterization of a wideband MEMS energy harvester utilizing nonlinear springs," *J. Micromech. Microeng.*, vol. 20, no. 12, p. 125009, Nov. 2010.

[18] B. P. Mann and B. A. Owens, "Investigations of a nonlinear energy harvester with a bistable potential well," *J. Sound Vibrat.*, vol. 329, no. 9, pp. 1215–1226, Apr. 2010.

[19] G. Despesse *et al.*, "High damping electrostatic system for vibration energy scavenging," in *Proc. SOC-EUSAI*, Grenoble, France, Oct. 2005, pp. 283–286.

[20] R. Guillemet, P. Basset, D. Galayko, F. Cottone, F. Marty, and T. Bourouina, "Efficient in-plane gap closing MEMS electrostatic vibration energy harvester," in *Proc. PowerMEMS*, Atlanta, GA, USA, Dec. 2012, pp. 137–140.

[21] Y. Chiu and V. F. G. Tseng, "A capacitive vibration-to-electricity energy converter with integrated mechanical switches," *J. Micromech. Microeng.*, vol. 18, no. 10, p. 104004, Jun. 2008.

[22] [Online]. Available: http://www.memscap.com/products/mumps/soimumps/reference-material, accessed Nov. 1, 2014.

[23] K. Yamashita, M. Honzumi, K. Hagiwara, Y. Iguchi, and Y. Suzuki, "Vibration-driven MEMS energy harvester with vacuum UV-charged vertical electrets," in *Proc. TRANSDUCERS*, Jun. 2011, pp. 2630–2633.

[24] D. S. Nguyen, N.-H. T. Tran, E. Halvorsen, and I. Paprotny, "Design and fabrication of MEMS electrostatic energy harvester with nonlinear springs and vertical sidewalls," in *PowerMEMS Tech. Dig.*, Seoul, Korea, Nov. 2011, pp. 126–129.

[25] C. P. Le, E. Halvorsen, O. Søråsen, and E. M. Yeatman, "Microscale electrostatic energy harvester using internal impacts," *J. Intell. Mater. Syst. Struct.*, vol. 23, no. 13, pp. 1409–1421, Feb. 2012.

[26] K. Matsumoto, K. Saruwatari, and Y. Suzuki, "Vibration-powered battery-less sensor node using MEMS electret generator," in *Proc. PowerMEMS*, Seoul, Korea, Nov. 2011, pp. 134–137.

[27] H. Liu, C. J. Tay, C. Quan, T. Kobayashi, and C. Lee, "Piezoelectric MEMS energy harvester for low-frequency vibrations with wideband operation range and steadily increased output power," *J. Micromech. Microeng.*, vol. 20, no. 5, pp. 1131–1142, Oct. 2011.

[28] H. Liu, L. Dhakar, and C. Lee, "Ultra-broadband electromagnetic MEMS vibration energy harvesting," *J. Phys., Conf. Ser.*, vol. 476, no. 1, p. 012049, 2013.

[29] D. S. Nguyen, E. Halvorsen, and I. Paprotny, "Bistable springs for wideband microelectromechanical energy harvesters," *Appl. Phys. Lett.*, vol. 102, no. 2, p. 023904, 2013.

[30] W.-M. Zhang, H. Yan, Z.-K. Peng, and G. Meng, "Electrostatic pull-in instability in MEMS/NEMs: A review," *Sens. Actuators A, Phys.*, vol. 214, pp. 187–218, Aug. 2014.

[31] C. P. Le and E. Halvorsen, "Electrostatic modeling of in-plane overlap energy harvesters," in *Proc. PowerMEMS*, Washington, DC, USA, Dec. 2009, pp. 336–339.

[32] D. C. Miller, B. L. Boyce, M. T. Dugger, T. E. Buchheit, and K. Gall, "Characteristics of a commercially available silicon-on-insulator MEMS material," *Sens. Actuators A, Phys.*, vol. 138, no. 1, pp. 130–144, Apr. 2007.

[33] M. Bao and H. Yang, "Squeeze film air damping in MEMS," *Sens. Actuators A, Phys.*, vol. 136, pp. 3–27, Jan. 2007.

[34] M.-H. Bao, "Micromechanical transducers: Pressure sensors, accelerometers and gyroscopes," in *Handbook of Sensors and Actuators*, vol. 8. Amsterdam, The Netherlands: Elsevier, 2000.

[35] E. Halvorsen, C. P. Le, P. D. Mitcheson, and E. M. Yeatman, "Architecture-independent power bound for vibration energy harvesters," *J. Phys., Conf. Ser.*, vol. 476, no. 1, p. 012026, 2013.

[36] M. J. Brennan, I. Kovacic, A. Carrella, and T. P. Waters, "On the jump-up and jump-down frequencies of the Duffing oscillator," *J. Sound Vibrat.*, vol. 318, pp. 1250–1261, Dec. 2008.

Sukhdeep Kaur received the B.Sc. degree in computer science and the M.Sc. degree in physics from Guru Nanak Dev University, Amritsar, India, in 2004 and 2006, respectively. She is currently pursuing the Ph.D. degree with the Department of Micro and Nano Systems Technology, Buskerud and Vestfold University College, Horten, Norway, with a focus on biasing methods and end-stop impacts in MEMS electrostatic energy harvesters.

Einar Halvorsen (M'03) received the Siv.Ing. degree in physical electronics and the Dr.Ing. degree in physics from the Norwegian University of Science and Technology, Trondheim, Norway, in 1991 and 1996, respectively. He has worked both in academia and the microelectronics industry. Since 2004, he has been with Buskerud and Vestfold University College, Horten, Norway, where he is currently a Professor of Micro- and Nanotechnology. His current main research interest is in theory, design, and modeling of microeletromechanical devices.

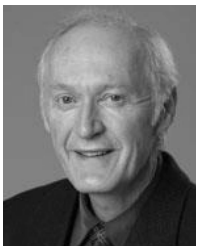

Oddvar Søråsen received the Cand.Real. degree in physics from the University of Oslo (UiO), in 1973. He started his career with the Norwegian Defence Research Establishment and was appointed as a Professor of VLSI Systems with the Department of Informatics, UiO, in 1986. During his academic period, he has served as the Head of the Department of Informatics and the Research Group Leader and is a Professor Emeritus with UiO. His research interests are computer system architecture, micro and nano electronics, and microelectromechanical devices.

Eric M. Yeatman has been a member of academic staff with Imperial College London at South Kensington Campus since 1989, and a Professor of Micro-Engineering since 2005. He is currently the Head of the Department of Electrical and Electronic Engineering, and a Fellow and Silver Medalist of the Royal Academy of Engineering. He is the Co-Founder and Director of Microsaic Systems plc, which develops and markets miniature mass spectrometers for portable chemical analysis. He has published widely in integrated optics, surface plasmon devices, MEMS 3-D self-assembly, and microenergy harvesting. His current research interests are in motion and thermal energy harvesting for wireless devices, pervasive sensing, and sensor networks.